Journal of Fluorine Chemistry 132 (2011) 660–668

Contents lists available at ScienceDirect

Journal of Fluorine Chemistry

journal homepage: www.elsevier.com/locate/fluor

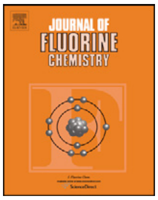

A Raman spectroscopic study of the $XeOF_4/XeF_2$ system and the X-ray crystal structure of α-$XeOF_4{\cdot}XeF_2$☆

Michael J. Hughes, David S. Brock, Hélène P.A. Mercier, Gary J. Schrobilgen *

Department of Chemistry, McMaster University, Hamilton, Ontario L8S 4M1, Canada

ARTICLE INFO

Article history:
Received 25 April 2011
Received in revised form 10 May 2011
Accepted 13 May 2011
Available online 23 May 2011

Keywords:
Weakly bonding interactions
Noble-gas chemistry
X-ray crystallography
Raman spectroscopy
Xenon oxide tetrafluoride
Xenon difluoride

ABSTRACT

The mixed oxidation state complexes, α-$XeOF_4{\cdot}XeF_2$ and β-$XeOF_4{\cdot}XeF_2$, result from the interaction of XeF_2 with excess $XeOF_4$. The X-ray crystal structure of the more stable α-phase shows that the XeF_2 molecules are symmetrically coordinated through their fluorine ligands to the Xe(VI) atoms of the $XeOF_4$ molecules which are, in turn, coordinated to four XeF_2 molecules. The high-temperature phase, β-$XeOF_4{\cdot}XeF_2$, was identified by low-temperature Raman spectroscopy in admixture with α-$XeOF_4{\cdot}XeF_2$; however, the instability of the β-phase precluded its isolation and characterization by single-crystal X-ray diffraction. The Raman spectrum of β-$XeOF_4{\cdot}XeF_2$ indicates that the oxygen atom of $XeOF_4$ interacts less strongly with the XeF_2 molecules in its crystal lattice than in α-$XeOF_4{\cdot}XeF_2$. The ^{19}F and ^{129}Xe NMR spectra of XeF_2 in liquid $XeOF_4$ at −35 °C indicate that any intermolecular interactions that exist between XeF_2 and $XeOF_4$ are weak and labile on the NMR time scale. Quantum-chemical calculations at the B3LYP and PBE1PBE levels of theory were used to obtain the gas-phase geometries and vibrational frequencies as well as the NBO bond orders, valencies, and NPA charges for the model compounds, $2XeOF_4{\cdot}XeF_2$, and $XeOF_4{\cdot}4XeF_2$, which provide approximations of the local XeF_2 and $XeOF_4$ environments in the crystal structure of α-$XeOF_4{\cdot}XeF_2$. The assignments of the Raman spectra (−150 °C) of α- and β-$XeOF_4{\cdot}XeF_2$ have been aided by the calculated vibrational frequencies for the model compounds. The fluorine bridge interactions in α- and β-$XeOF_4{\cdot}XeF_2$ are among the weakest for known compounds in which XeF_2 functions as a ligand, whereas such fluorine bridge interactions are considerably weaker in β-$XeOF_4{\cdot}XeF_2$.

1. Introduction

The noble-gas difluorides, NgF_2, behave as fluoride ion donors towards strong fluoride ion acceptors such as MF_5 (M = As, Sb, Bi) forming NgF^+ salts that have shortened Ng–F bonds relative to their parent NgF_2 molecules [1–8]. In such cases, a fluoride ion of NgF_2 is essentially transferred to form $[NgF][MF_6]$. A fluorine ligand of the anion, however, interacts with the NgF^+ cation by means of a long Ng---F fluorine bridge bond, forming an ion pair, e.g., $F{-}Ng^+{-}{-}{-}F{-}AsF_5^-$ [2,8]. In contrast, coordination of a weak to moderate strength, oxidatively resistant Lewis acid to a fluorine atom of NgF_2 occurs without "complete" fluoride ion transfer. A considerable number of metal cations exhibiting this behavior towards XeF_2 have been synthesized and structurally characterized. Recent reviews outlining progress in this area [9,10] show a considerable range of coordination behaviors as exemplified by $[M(XeF_2)_5][PF_6]_2$ (M = Ca, Cd) [11], $[Pb_3(XeF_2)_{11}][PF_6]_6$ [12], $[M(XeF_2)_3][PF_6]_2$ (M = Sr, Pb) [12], $[Sr_3(XeF_2)_{10}][PF_6]_6$ [12], $[Ba(XeF_2)_5][AsF_6]_2$ [13], and $[Ba(XeF_2)_4][PF_6]_2$ [14]. In such cases, the XeF_2 ligand may be coordinated through one or both of its fluorine atoms to give adducts in which XeF_2 is terminal or bridging. Terminal coordination of XeF_2 results in lengthening of the Xe–F bridge bond and contraction of the terminal Xe–F bond, whereas bridging XeF_2 ligands can be either symmetrically or asymmetrically coordinated. Terminal coordination or significantly distorted bridge-coordinated XeF_2 results in two Xe–F stretching bands in the Raman spectrum, one shifted to lower frequency for the longer Xe–F bond and one to higher frequency for the shorter Xe–F bond. Symmetrical bridge coordination results in a single symmetric XeF_2 stretching band in the Raman spectrum which is shifted to higher frequency relative to uncoordinated XeF_2.

Examples of XeF_2 coordinated to moderate strength Lewis acid transition metal oxide fluorides have also been reported. Adducts of XeF_2 with MOF_4 (M = Mo, W), $XeF_2{\cdot}nMOF_4$ (n = 1–4) are known and have been characterized by solution ^{19}F and ^{129}Xe NMR spectroscopy [15,16], Raman spectroscopy [16,17], and X-ray crystallography [18]. Several examples in which XeF_2 coordinates to non-metal cations are also known and these are represented by $2XeF_2{\cdot}[XeF_5][AsF_6]$ [19], $XeF_2{\cdot}[XeF_5][AsF_6]$ [19], and $XeF_2{\cdot}2([XeF_5][AsF_6])$ [19], where XeF_2 coordinates to the

---

☆ Dédié au Professeur Alain Tressaud, notre collègue et ami, pour l'obtention du ACS Award for Creative Work in Fluorine Chemistry (2011).

* Corresponding author.
E-mail address: schrobil@mcmaster.ca (G.J. Schrobilgen).

0022-1139/$ – see front matter © 2011 Elsevier B.V. All rights reserved.
doi:10.1016/j.jfluchem.2011.05.010

Xe(VI) atom of XeF_5^+. Recently, the X-ray crystal structures of $[BrOF_2][AsF_6]\cdot 2NgF_2$ (Ng = Kr [20], Xe [21]) have been reported which contain NgF_2 molecules that are terminally coordinated to bromine(V) through fluorine. The Ng–F stretching frequencies of main-group cation complexes with NgF_2 show frequency shift patterns that are similar to those of the metal cation complexes (vide supra).

The compound, $XeOF_4\cdot XeF_2$, was first synthesized by Bartlett et al. who reported its Raman spectrum (−10 °C) and X-ray powder diffraction pattern [22]. The Raman spectrum was assigned as the sum of the component of XeF_2 and $XeOF_4$ spectra. A comparison of the unit cells and vibrational frequencies associated with $XeOF_4\cdot XeF_2$ and isoelectronic $IF_5\cdot XeF_2$ [23] led Bartlett et al. to suggest that the two compounds are likely isostructural and to categorize $XeOF_4\cdot XeF_2$ as a molecular addition compound. The crystal structure of $XeF_4\cdot XeF_2$ has also been reported and shows no evidence for weak covalent interactions between Xe(IV) and the fluorine ligands of XeF_2 [24].

The present paper details the formation and characterization of α-$XeOF_4\cdot XeF_2$ by single-crystal X-ray diffraction and of α- and β-$XeOF_4\cdot XeF_2$ by Raman spectroscopy. Quantum-chemical calculations have also been used to assign the vibrational spectra of α-$XeOF_4\cdot XeF_2$, in light of the X-ray crystal structure and a factor-group analysis, and of β-$XeOF_4\cdot XeF_2$.

2. Results and discussion

2.1. Syntheses of α- and β-$XeOF_4\cdot XeF_2$

Fusion of a 2:1 molar ratio of liquid $XeOF_4$ and solid XeF_2 resulted in a mixture of α- and β-$XeOF_4\cdot XeF_2$ (vide infra), with the relative proportions of the α- and β-phases depending on the crystallization conditions. When a mixture of XeF_2 and $XeOF_4$ was completely liquefied at 22 °C and then rapidly quenched to −78 °C, a mixture of $XeOF_4$, the more stable α-$XeOF_4\cdot XeF_2$ phase (see Section 2.3), and the less stable β-$XeOF_4\cdot XeF_2$ phase (see Section 2.4) resulted. When the sample was maintained at −78 °C for 20 h, the low-temperature Raman spectrum showed that the β-phase had completely converted to the more stable α-phase. Alternatively, when the aforementioned solid mixture was reliquefied, such that several crystallites remained suspended in the medium, and then rapidly quenched to −78 °C, the solid product primarily consisted of the α-phase with only a minor amount of β-$XeOF_4\cdot XeF_2$. The facile transition of β-$XeOF_4\cdot XeF_2$ to α-$XeOF_4\cdot XeF_2$ has prevented characterization of the β-phase by single-crystal X-ray diffraction.

The fusion of 1:1 and 1:2 molar ratios of $XeOF_4$ and XeF_2 and subsequent quenching to −78 °C resulted in α-$XeOF_4\cdot XeF_2$ (m.p., 26–28 °C) and unassociated XeF_2 in the case of the 1:2 molar ratio, with no other products observed by Raman spectroscopy. In the reaction involving a molar excess of XeF_2, the additional XeF_2 only partially dissolved with periodic mixing at temperatures up to 50 °C over a period of 5 h.

2.2. NMR spectroscopy

The ^{19}F [1] and ^{129}Xe [2] NMR spectra of XeF_2 (0.0203 g, 0.120 mmol) dissolved in $XeOF_4$ (0.5 mL) were recorded at −35 °C (XeF_2; 0.23 mol L^{-1}). Xenon difluoride and $XeOF_4$ showed spin–spin couplings and chemical shifts that are characteristic of the uncomplexed molecules. The ^{19}F chemical shift of XeF_2 (−183.0 ppm) is similar to that of XeF_2 in BrF_5 solvent (−181.8 ppm, 26 and −20 °C) [25] and the ^{129}Xe chemical shift (−1606 ppm) is similar to that recorded in HF (−1592 ppm; 25 °C) [26] and is shifted to somewhat lower frequency than in BrF_5 solvent (−1708 ppm; −40 °C) [26]. The $^{1}J(^{129}Xe–^{19}F)$ coupling constant of XeF_2 in $XeOF_4$ solvent (5630 Hz) is similar to those of XeF_2 in BrF_5 (5616 Hz, 26 °C [25]; 5650 Hz, −20 °C [25]; and 5583 Hz; −40 °C [26]) and in HF (5652 Hz, 25 °C) [26]. The ^{19}F and ^{129}Xe chemical shifts and the $^{1}J(^{129}Xe–^{19}F)$ coupling constants of $XeOF_4$ in the XeF_2 solution (98.1 and 6.5 ppm, 1120 Hz, respectively) are comparable to those of liquid $XeOF_4$ recorded at 24 °C (100.3 and 0.0 ppm, 1128 Hz, respectively) [27].

The NMR spectra indicate that any Xe(II)–F···Xe(VI) fluorine bridge interactions that may exist in solution are weak and labile. Moreover, no additional spin–spin couplings were observed that were indicative of strong Xe(II)–F···Xe(VI) fluorine bridge interactions.

2.3. X-ray crystal structure of α-$XeOF_4\cdot XeF_2$

Details of data collection parameters and other crystallographic information are provided in Table 1. Bond lengths and bond angles for $XeOF_4\cdot XeF_2$ are listed in Table 2. The unit cell parameters for α-$XeOF_4\cdot XeF_2$ are in good agreement with those obtained from the X-ray powder diffraction study (a = 7.56(2), c = 11.36(3) Å, V = 647 Å^3, Z = 4, 20 °C) [22].

2.3.1. Packing and intermolecular contacts

The α-$XeOF_4\cdot XeF_2$ complex crystallizes in the $I4/m$ space group. The structure of $XeOF_4\cdot XeF_2$ consists of $XeOF_4$ and XeF_2 units that stack along the a- and b-axes but alternate along the c-axis. The Xe–O bonds of $XeOF_4$ alternate their directions by 180° in columns along the a- and c-axes so that in the b, c-plane, either the Xe–O bonds or the xenon valence electron lone pairs of the $XeOF_4$ molecules face one another (Fig. S1). The XeF_2 ligands pack along the a- and b-axes alternating their orientations by 90°. There are four XeF_2 molecules that have close contacts with the Xe(VI) atom of $XeOF_4$ (Fig. 1a). In turn, each fluorine atom of the XeF_2 molecule has close contacts with the xenon atoms of two $XeOF_4$ molecules (Fig. 1b). The X-ray crystal structure confirms that α-$XeOF_4\cdot XeF_2$ is isostructural with $IF_5\cdot XeF_2$ [23]. The Xe···F contact distances in $XeOF_4\cdot XeF_2$ (3.239(4) Å) are comparable to the I···F contact distances in $IF_5\cdot XeF_2$ (3.142(7) Å), which are somewhat less than the sums of their respective Xe (3.63 Å)/I (3.45 Å) and F van der Waals radii [28]. Symmetric coordination of four XeF_2 molecules to Xe(VI) preserves the local C_{4v} symmetry of the $XeOF_4$ molecule, whereas symmetric coordination of one XeF_2 molecule to four $XeOF_4$ molecules results in local C_i symmetry at XeF_2, thus retaining the center of symmetry in XeF_2. The Xe···F contacts are shorter than those in $XeF_4\cdot XeF_2$ (3.353(7), 3.355(7) and 3.37(1) Å)

Table 1

Summary of crystal data and refinement results for α-$XeOF_4\cdot XeF_2$.

Chem formula	Xe_2OF_6
Space group	$I4/m$ (87)
a (Å)	7.502(1)
c (Å)	11.193(4)
V (Å^3)	630.0(6)
Molecules/unit cell	4
Mol wt (g mol^{-1})	1570.40
Calcd density (g cm^{-3})	4.139
T (°C)	−173
μ (mm^{-1})	10.81
R_1[a]	0.0257
wR_2[b]	0.0395

[a] R_1 is defined as $\Sigma||F_o| - |F_c||/\Sigma|F_o|$ for $I > 2\sigma(I)$.

[b] wR_2 is defined as $\{\Sigma[w(F_o^2 - F_c^2)^2]/\Sigma w(F_o^2)^2\}^{1/2}$ for $I > 2\sigma(I)$.

---

[1] Fluorine-19 resonances assigned to traces of XeF_4 [XeO_2F_2] {HF} impurities were observed at −18.4 ppm, $^{1}J(^{19}F–^{129}Xe)$ = 3848 Hz; [101.1 ppm, $^{1}J(^{19}F–^{129}Xe)$ = 1180 Hz]; and {−188.7 ppm}.

[2] Xenon-129 resonances assigned to trace XeF_4 [XeO_2F_2] impurities were observed at 287 ppm, $^{1}J(^{19}F–^{129}Xe)$ = 3848 Hz and [127 ppm, $^{1}J(^{19}F–^{129}Xe)$ = 1180 Hz)].

Table 2
Experimental bond lengths and bond angles in α-$XeOF_4{\cdot}XeF_2$ and calculated bond lengths and angles in $2XeOF_4{\cdot}XeF_2$ and $XeOF_4{\cdot}4XeF_2$.

α-$XeOF_4{\cdot}XeF_2$[a]		$2XeOF_4{\cdot}XeF_2$[b]			$XeOF_4{\cdot}4XeF_2$[c]		
Exptl		Calcd (C_{2h})[d]			Calcd (C_4)[d]		
			B3LYP	PBE1PBE		B3LYP	PBE1PBE
		Bond lengths (Å)					
Xe(1)–O(1)	1.729(7)	$Xe_1–O_1$	1.742	1.725	$Xe_1–O_1$	1.744	1.727
Xe(1)–F(1)	1.900(3)	$Xe_1–F_{1,2}$	1.960	1.935	$Xe_1–F_{1,2,3,4}$	1.953	1.928
		$Xe_1–F_{3,4}$	1.952	1.925			
Xe(1)···F(2)	3.239(4)	$Xe_1\cdots F_5$	2.880	2.890	$Xe_1\cdots F_{5,7,9,11}$	3.446	3.357
Xe(2)–F(2)	2.014(5)	$Xe_2–F_5$	2.024	1.999	$Xe_{2,3,4,5}–F_{5,7,9,11}$	2.031	2.006
					$Xe_{2,3,4,5}–F_{6,8,10,12}$	2.004	1.979
		Bond angles (°)					
O(1)–Xe(1)–F(1)	89.2(1)	$O_1–Xe_1–F_{1,2}$	92.2	91.6	$O_1–Xe_1–F_{1,2,3,4}$	90.8	90.3
		$O_1–Xe_1–F_{3,4}$	92.4	91.8			
O(1)–Xe(1)···F(2)	141.13(8)	$O_1–Xe_1\cdots F_5$	162.0	158.0	$O_1–Xe_1\cdots F_{5,7,9,11}$	139.5	139.4
F(1)–Xe(1)–F(1C)	89.988(3)	$F_1–Xe_1–F_2$	88.9	88.8	$F_1–Xe_1–F_2$	90.0	90.0
F(1)–Xe(1)–F(1B)	89.988(3)	$F_1–Xe_1–F_4$	90.2	90.2	$F_1–Xe_1–F_4$	90.0	90.0
F(1)–Xe(1)–F(1A)	178.3(2)	$F_1–Xe_1–F_3$	175.4	176.5	$F_1–Xe_1–F_3$	178.4	179.4
F(1)–Xe(1)···F(2)	60.6(1)	$F_1–Xe_1\cdots F_5$	75.1	73.0	$F_1–Xe_1\cdots F_5$	60.6	61.4
F(1)–Xe(1)···F(2D)	68.6(1)				$F_1–Xe_1\cdots F_7$	63.5	63.4
F(1)–Xe(1)···F(2B)	120.9(1)				$F_1–Xe_1\cdots F_9$	118.0	118.1
F(1)–Xe(1)···F(2F)	141.1(1)				$F_1–Xe_1\cdots F_{11}$	115.2	116.1
		$F_3–Xe_1–F_4$	90.4	90.6			
		$F_3–Xe_1\cdots F_5$	100.2	103.6			
F(2)–Xe(2)–F(2A)	180.000(1)	$F_5–Xe_2–F_5'$	180.0	180.0	$F_{5,7,9,11}–Xe–F_{6,8,10,12}$	179.0	179.0
Xe(1)···F(2)–Xe(2)	116.8(1)	$Xe_1\cdots F_5–Xe_2$	127.5	122.7	$Xe_1\cdots F_{5,7,9,11}–Xe_{2,3,4,5}$	116.6	117.3

[a] For the atom labeling scheme, see Fig. 1.
[b] For the atom labeling scheme, see Fig. 4b.
[c] For the atom labeling scheme, see Fig. 4a.
[d] The aug-cc-pVTZ(-PP) basis sets were used.

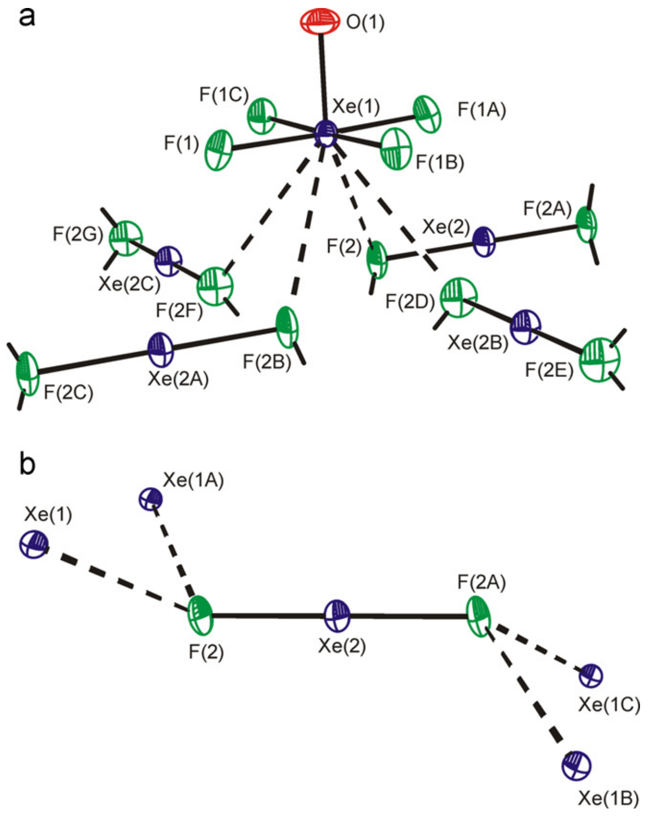

Fig. 1. Depictions of the coordination spheres of (a) $XeOF_4$ and (b) XeF_2 in the X-ray crystal structure of α-$XeOF_4{\cdot}XeF_2$; the thermal ellipsoids are drawn at the 50% probability level.

[24], indicating that $XeOF_4$ and XeF_2 interact by means of weak polar-covalent fluorine bridge interactions in α-$XeOF_4{\cdot}XeF_2$.

2.3.2. $XeOF_4$ geometry and coordination

The $XeOF_4$ molecule is based on a pseudo-octahedral AX_4YE VSEPR arrangement of four bond pairs (X), a double bond pair (Y), and a valence electron lone pair (E) which give rise to a square-pyramidal geometry. The four fluorine atoms that comprise the base of the square pyramid are coplanar as imposed by symmetry, with the apical oxygen atom located 1.701 Å above the equatorial plane and the xenon atom 0.028 Å below that plane.

The Xe(1)···F(2) contact interactions that occur between $XeOF_4$ and XeF_2 are somewhat less than the sum of the xenon and fluorine van der Waals radii [28] and result in nine-coordinate Xe(VI) atoms (Fig. 1a). The Xe(VI)···F contacts occur from beneath the equatorial plane of the $XeOF_4$ molecule, avoiding the valence electron lone pair position in a manner similar to that described for $[XeF_5][RuF_6]$ [29], $[XeF_5][OsO_3F_3]$ [30], and $[XeF_5][\mu\text{-}F(OsO_3F_2)_2]$ [30]. The secondary contacts in $XeOF_4{\cdot}XeF_2$ occur between four F(2) atoms of four symmetry-equivalent XeF_2 molecules and the Xe(1) atom, which is located 2.522 Å above the F(2,2B,2D,2F)-plane. This plane is parallel to the equatorial F(1,1A,1B,1C)-plane formed by the primary Xe(VI)–F bonds. The light atom intraplanar distances (F(1)···F(1B), 2.687(5) Å; F(2)···F(F2D), 2.875(4) Å) are comparable to the interplanar distances (F(1)···F(2), 2.839(4) Å; F(1)···F(2D), 3.101(4) Å), and are significantly longer than the O(1)···F(1) distance (2.550(6) Å). The planes, when viewed along the Xe–O bond axis (Fig. 2), have a gauche conformation so that the Xe(VI) coordination sphere may be described as a distorted monocapped square antiprism having dihedral angles between the basal fluorine atom planes of the $XeOF_4$ molecules and the planes of contacting fluorine atoms (36.8° for the F(2,2B)Xe(1)O(1)- and F(1,1A)Xe(1)O(1)-planes and 53.2° for the F(2D,2F)Xe(1)O(1)- and F(1,1A)Xe(1)O(1)-planes of $XeOF_4{\cdot}XeF_2$). The Xe–F bond lengths of $XeOF_4$ (1.900(3) Å) are not significantly affected by the long secondary Xe(VI)···F contacts and are similar to those of other

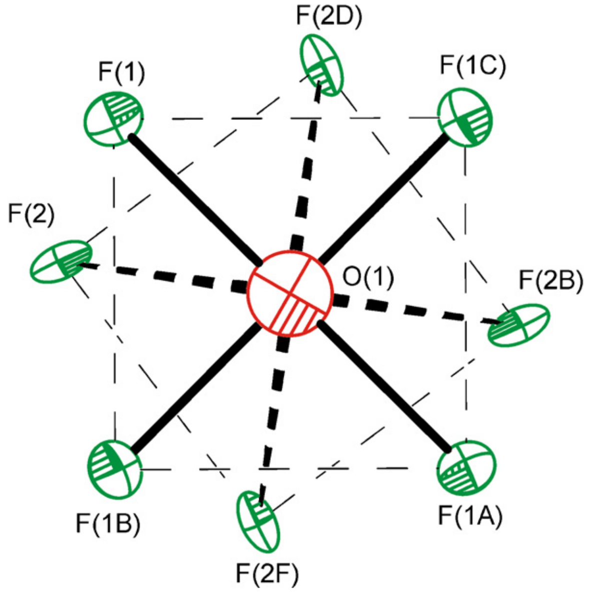

Fig. 2. A depiction of the light atom coordination sphere of Xe(VI) in α-$XeOF_4{\cdot}XeF_2$; the thermal ellipsoids are drawn at the 50% probability level.

structures containing coordinated $XeOF_4$; e.g., $[XeF_5][SbF_6]{\cdot}XeOF_4$ (1.890(2) and 1.895(2) Å) [31] and $(OsO_3F_2)_2{\cdot}2XeOF_4$ (1.907(5)–1.918(5) Å) [32] as well as the gas-phase electron diffraction structure of $XeOF_4$ (1.901(3) Å) [33]. The Xe–O bond length of α-$XeOF_4{\cdot}XeF_2$ (1.729(7) Å) is similar to those of $[XeF_5][SbF_6]{\cdot}XeOF_4$ (1.713(3) Å) [31], $(OsO_3F_2)_2{\cdot}2XeOF_4$ (1.709(6) Å) [32], and gaseous $XeOF_4$ (electron diffraction, 1.71(1) Å) [33].

2.3.3. XeF_2 geometry and coordination

The XeF_2 molecule in α-$XeOF_4{\cdot}XeF_2$ is linear by symmetry with Xe–F bond lengths of 2.014(5) Å. The Xe–F bond lengths are slightly elongated when compared with those obtained from the rotational fine structure in the gas-phase Raman (1.9791(1) Å) [34] and infrared (1.977965(5) Å) [35] gas-phase spectra of XeF_2, and are comparable to the Xe–F bond lengths obtained from the X-ray crystal structure (1.999(4) Å) [8], and neutron diffraction structure (2.00(1) Å) [36] of XeF_2. They are in good agreement with other compounds containing symmetrically coordinated XeF_2 molecules; e.g., $IF_5{\cdot}XeF_2$ (2.018(9) Å) [23], $2[XeF_5][AsF_6]{\cdot}XeF_2$ (2.01(2) Å) [19], $XeF_4{\cdot}XeF_2$ (2.010(6) Å) [24], and $[Ba(XeF_2)_5][AsF_6]_2$ (1.994(9), 2.005(5), and 1.995(5) Å) [14].

2.4. Raman spectroscopy

The low-temperature Raman spectrum of α-$XeOF_4{\cdot}XeF_2$ (Fig. 3) was obtained by dissolution of XeF_2 in an equimolar amount of $XeOF_4$ at 50 °C. However, dissolution of XeF_2 in a molar excess of $XeOF_4$ at 22 °C led to the formation of varying amounts of $XeOF_4{\cdot}XeF_2$ in admixture with $XeOF_4$, with the ratio of α- and β-$XeOF_4{\cdot}XeF_2$ dependent on the crystallization conditions (see Fig. 4 and Section 2.1). The frequencies and their assignments for α- and β-$XeOF_4{\cdot}XeF_2$ are listed in Table 3.

The assignments and mode descriptions were arrived at by comparison with the experimental and calculated frequencies of gas-phase (Table S1) and solid (Fig. S2) $XeOF_4$ and XeF_2 (Table S2), along with the calculated gas-phase frequencies and mode descriptions for the unknown model compounds, $2XeOF_4{\cdot}XeF_2$ (C_{2h}) (Table S3) and $XeOF_4{\cdot}4XeF_2$ (C_1) (Table S4). The energy-minimized geometries of the model compounds were calculated, providing close approximations to the local symmetries of the $XeOF_4$ ($XeOF_4{\cdot}4XeF_2$) and XeF_2 ($2XeOF_4{\cdot}XeF_2$) molecules in the crystal structure of α-$XeOF_4{\cdot}XeF_2$, allowing an estimation of the degree of intra- and intermolecular vibrational coupling and for comparison of their frequency shifts with respect to those calculated for gas-phase $XeOF_4$ and XeF_2. The geometric parameters of these adducts and their benchmark molecules calculated at the PBE1PBE level provided the best overall agreement with experiment (see Section 2.5) and are therefore referred to in the ensuing discussion.

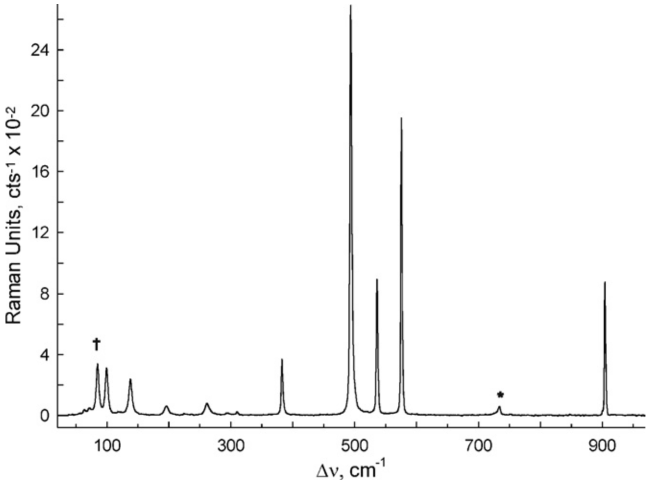

Fig. 3. Raman spectrum of α-$XeOF_4{\cdot}XeF_2$ recorded at −150 °C using 1064-nm excitation; the symbols denote FEP sample tube lines (*) and an instrumental artifact (†).

2.4.1. α-$XeOF_4{\cdot}XeF_2$

The Raman spectrum of α-$XeOF_4{\cdot}XeF_2$ (Fig. 3) has been previously reported [22]. The present work provides more detailed assignments and descriptions of the vibrational modes based on a knowledge of the crystal structure. The spectrum is relatively simple and is comprised of nine bands and is basically a composite of $XeOF_4$ and XeF_2 spectra. In view of the very weak Xe(VI)···F and Xe(II)···F interactions, a modified factor-group analysis was carried out for $XeOF_4$ and XeF_2 in the crystal structure of α-$XeOF_4{\cdot}XeF_2$ (Table S5) which indicates that site symmetry reduction and correlation to the unit cell symmetry for each component should lead to additional band splittings. Failure to observe these factor-group splittings implies that the vibrational couplings within the unit cell are weak and too small to be resolved.

The local crystallographic symmetry of XeF_2 in α-$XeOF_4{\cdot}XeF_2$ is C_i and results in two crystallographically equivalent Xe–F bond lengths (vide supra). As in uncomplexed XeF_2, only the band derived from the symmetric XeF_2 stretch, $\nu(Xe_2F_5) + \nu(Xe_2F_5')$, is Raman active (494 cm^{-1}) with a frequency similar to that of uncomplexed XeF_2 (497 cm^{-1}) [38]. Similar frequencies have been reported for XeF_2 in $IF_5{\cdot}XeF_2$ (493 cm^{-1}) [39] and $2[XeF_5][AsF_6]{\cdot}XeF_2$ (496 cm^{-1}) [19], where XeF_2 is bridging but only weakly coordinated. More pronounced complexation shifts have been observed for $[Ag(XeF_2)_2][AsF_6]$ (501, 508 cm^{-1}) [40], $[Ba(XeF_2)_5][SbF_6]_2$ (521 cm^{-1}) [41], and $[M(XeF_2)_3][AsF_6]_2$ [M = Pb (514 cm^{-1}) or Sr (531 cm^{-1})] [42] where the bridging XeF_2 molecule is more strongly coordinated. It is noteworthy that the calculated values for $\nu(XeF_5) - \nu(XeF_5')$ (535 cm^{-1}) and $\delta(F_5XeF_5')$ (220, 238 cm^{-1}) are in good agreement with the experimental gas-phase infrared values of uncomplexed XeF_2 (555 and 213 cm^{-1}, respectively). Within the range of experimentally observed frequencies, only two modes are predicted to display vibrational coupling between the $XeOF_4$ and XeF_2 molecules. These are predicted to occur at 576 and 282 cm^{-1} (Table S3) and both are

Table 3

Raman frequencies and intensities for $XeOF_4$, XeF_2, α-, and β-$XeOF_4{\cdot}XeF_2$; and assignments based on those of $XeOF_4{\cdot}4XeF_2$ and $2XeOF_4{\cdot}XeF_2$ (Tables S3 and S4).

exptl[a]			assgnts[b]
$XeOF_4$[c]	α-$XeOF_4{\cdot}XeF_2$[d,e]	β-$XeOF_4{\cdot}XeF_2$[d,f]	$XeOF_4{\cdot}4XeF_2$ (C_4)[g]
928(m)	904(30)	924(16) 920sh	A, $\nu(Xe_1O_1)$
609(vw)		609(2)	E, $\nu(Xe_1F_1) - \nu(Xe_1F_3)$ / $\nu(Xe_1F_2) - \nu(Xe_1F_4)$
577(vs)	575(72)	564(51) 560(15) 554(9) 550(6)	A, $\nu_s(Xe_1F_{4e})$
543(w)	536(33)	527(30) 525(27)	B, $[\nu(Xe_1F_1) + \nu(Xe_1F_2)] - [\nu(Xe_1F_4) + \nu(Xe_1F_3)]$[h]
		517(7)	B, $[\nu(Xe_1F_1) + \nu(Xe_1F_2)] - [\nu(Xe_1F_4) + \nu(Xe_1F_3)]$[i]
360(w)	383(14)	372sh 370(8) 363(4) 361(4)	E, $\delta(O_1Xe_1F_1F_4)$ / $\delta(O_1Xe_1F_2F_3)$
286(m)	262(3)	234(4)	A, $\delta_{umb}(Xe_1F_{4e})$
225(w)	196(2)	223sh	B, $\delta(F_1Xe_1F_2) + \delta(F_3Xe_1F_4)$[j] B, $\delta(F_1Xe_1F_2) + \delta(F_3Xe_1F_4)$[k]
161(w)			E, $\delta(F_1Xe_1F_3)$ / $\delta(F_2Xe_1F_4)$
	99(12)	91sh	E, $\rho_r(XeOF_4)$
			B, $\rho_t(F_1Xe_1F_2) - \rho_t(F_3Xe_1F_4)$
			A, $\rho_t(Xe_1F_{4e})$
XeF_2[l]			$2XeOF_4{\cdot}XeF_2$ (C_{2h})[m]
	i.a.	i.a.	B_u $\nu(Xe_2F_5) - \nu(Xe_2F_5')$
	i.a.	i.a.	B_u $\nu(Xe_2F_5) - \nu(Xe_2F_5')$[n]
497(100)	494(100)	503(100)	A_g $\nu(Xe_2F_5) + \nu(Xe_2F_5')$
	i.a.	i.a.	B_u $\delta(F_5Xe_2F_5')$[o]
	i.a.	i.a.	B_u $\delta_{ip}(F_5Xe_2F_5')$
	i.a.	i.a.	A_u $\delta_{oop}(F_5Xe_2F_5')$
	138(9)		A_g $\rho_r(F_5Xe_2F_5')_{ip}$

[a] Frequencies are given in cm^{-1}.

[b] The abbreviations denote stretch (ν), symmetric (s) bend (δ), twist (ρ_t), rotation (ρ_r), umbrella (δ_{umb}), in-plane (ip), out-of-plane (oop), F(1)F(1A)F(1B)F(1C) (F_{4e}).

[c] From ref [37]. The abbreviations denote very strong (vs), medium (m), weak (w), and very weak (vw).

[d] The Raman spectrum was recorded on a microcrystalline solid sample in a FEP tube at −150 °C using 1064-nm excitation. Experimental Raman intensities are given in parentheses and are relative intensities with the most intense band given as 100. The abbreviations denote shoulder (sh), broad (br), inactive (i.a.) and not observed (n.o.).

[e] The sample had been allowed to stand for 20 h at −78 °C. A weak band was also observed at 310(1) cm^{-1} but was unassigned.

[f] The spectrum was recorded immediately after quenching the sample from 22 to −78 °C. Bands associated to $XeOF_4$ were also observed at 900(sh), 588(14), 542(13), 532(28), 368(sh) and 250(2) cm^{-1}. Bands associated to α-$XeOF_4{\cdot}XeF_2$ were also observed at 903(67), 575(151), 535(74), 493(201), 382(28), 261(6), 195(4), 137(17) and 98(23) cm^{-1}. A weak band was also observed at 309(1) cm^{-1} but was unassigned.

[g] See Fig. 4a for the atom labeling scheme. See Table S4 for complete mode descriptions and calculated frequencies for $XeOF_4{\cdot}XeF_2$.

[h] Also out-of-phase coupled to $[\nu(Xe_2F_5) + \nu(Xe_4F_9)] - [\nu(Xe_3F_7) + \nu(Xe_5F_{11})]$.

[i] Also in-phase coupled to $[\nu(Xe_2F_5) + \nu(Xe_4F_9)] - [\nu(Xe_3F_7) + \nu(Xe_5F_{11})]$.

[j] Also coupled to $[\delta(F_5Xe_2F_6) + \delta(F_9Xe_4F_{10})] - [\delta(F_7Xe_3F_8) + \delta(F_{11}Xe_5F_{12})]$.

[k] Also coupled to $[\rho_w(F_7Xe_3F_8) + \rho_w(F_{11}Xe_5F_{12})] - [\rho_w(F_5Xe_2F_6) + \rho_w(F_9Xe_4F_{10})]$.

[l] From ref. [38].

[m] See Fig. 4b for the atom labeling scheme. See Table S3 for the complete mode descriptions and calculated frequencies for $2XeOF_4{\cdot}XeF_2$.

[n] Also coupled to $[\nu(XeF_1) + \nu(XeF_2) + \nu(XeF_3) + \nu(XeF_4)] - [\nu(Xe'F_1') + \nu(Xe'F_2') + \nu(Xe'F_3') + \nu(Xe'F_4')]$.

[o] Also coupled to $\delta_{umb}(Xe'F_1'F_2'F_3'F_4') - \delta_{umb}(XeF_1F_2F_3F_4)$.

predicted to be Raman inactive. The band at 138 cm^{-1} is assigned to $\rho_r(F_5XeF_5')$ of the weakly coordinated XeF_2 molecule.

The $XeOF_4$ molecule in crystalline α-$XeOF_4{\cdot}XeF_2$ is also symmetrically coordinated and has local C_{4v} symmetry. The Xe–O stretch (904 cm^{-1}) is shifted to lower frequency relative to that of the gas-phase molecule (928 cm^{-1}) [37]. The calculated shift for ν(XeO) in $XeOF_4{\cdot}4XeF_2$ (930 cm^{-1}) relative to that calculated for $XeOF_4$ (936 cm^{-1}) (Table S1) is also to lower frequency but is smaller than the experimental complexation shift. This shift presumably results from interactions between oxygen atoms of $XeOF_4$ and the Xe(II) atoms of neighboring XeF_2 molecules which serve to stabilize the negative charge on the oxygen atom, thereby decreasing the Xe(VI)–O double bond character (vide infra). The band at 575 cm^{-1} is assigned to $\nu_s(Xe_1F_{4e})$ and is comparable to the corresponding mode in gas-phase $XeOF_4$ (577 cm^{-1}) [37], whereas the calculated $\nu_s(Xe_1F_{4e})$ frequency (569 cm^{-1}) in $XeOF_4{\cdot}4XeF_2$ is predicted to be shifted relative to that calculated for $XeOF_4$ (583 cm^{-1}) in the gas phase. The band at 536 cm^{-1} is assigned to the asymmetric Xe–F stretching mode and is shifted to lower frequency relative to that of gaseous $XeOF_4$ (543 cm^{-1}) [37]. A similar low-frequency shift is observed for the deformation mode, $\delta(F_1Xe_1F_2) + \delta(F_3Xe_1F_4)$, which occurs at 196 cm^{-1} compared to that of gas phase $XeOF_4$ (225 cm^{-1}) [37]. Although the calculated model does not perfectly reproduce the experimental spectrum, it does provide a very close approximation to the local symmetry at the $XeOF_4$ center. The only band in the α-$XeOF_4{\cdot}XeF_2$ spectrum that does not have a counterpart in the gas-phase infrared or Raman spectra of gaseous $XeOF_4$ or solid XeF_2 occurs at 99 cm^{-1} and has been assigned to $\rho_r(XeOF_4)$, in reasonable agreement with the calculated value of 88 cm^{-1}.

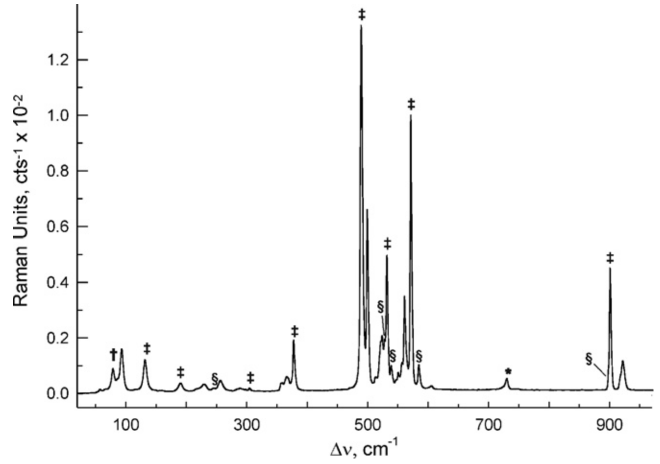

Fig. 4. Raman spectrum of a mixture of α-$XeOF_4 \cdot XeF_2$ (‡), β-$XeOF_4 \cdot XeF_2$ (unlabeled bands), and $XeOF_4$ (§) recorded at −150 °C using 1064-nm excitation; FEP sample tube lines (*) and an instrumental artifact (†) are also indicated.

2.4.2. β-$XeOF_4 \cdot XeF_2$

The bands in the Raman spectrum of β-$XeOF_4 \cdot XeF_2$ (Fig. 4) occur at frequencies that are similar to those in α-$XeOF_4 \cdot XeF_2$, suggesting that the two phases have similar structures. In contrast with α-$XeOF_4 \cdot XeF_2$, many of the bands are split, but in the absence of a crystal structure, it is not possible to comment on the precise origins of the band splittings or frequency differences.

The Xe–O and Xe–F stretching frequencies of $XeOF_4$ are shifted to higher (920, 924 cm^{-1}) and lower (550, 554, 560, 564, cm^{-1}) frequencies, respectively, when compared with those of α-$XeOF_4 \cdot XeF_2$ (904 and 575 cm^{-1}, respectively). These shifts presumably result from a decrease in, or the absence of, the intermolecular Xe(II)···O interactions that exist in α-$XeOF_4 \cdot XeF_2$. Each oxygen atom in the crystal structure of α-$XeOF_4 \cdot XeF_2$ has four weak interactions with four Xe(II) atoms of four neighboring XeF_2 molecules (3.985 Å compared to $\Sigma_{\text{vdW (Xe–O)}}$ = 3.68 Å) [28] and one repulsive contact with one oxygen atom of another $XeOF_4$ molecule (2.691 Å compared to $\Sigma_{\text{vdW (O–O)}}$ = 3.04 Å) [28]. Besides the Xe(1)···F(2) interactions (see Section 2.3), these weak interactions may contribute to reduce the Xe–O double bond character and account for the lower ν(XeO) frequency (904 cm^{-1}) in α-$XeOF_4 \cdot XeF_2$ relative to that of gaseous $XeOF_4$ (928 cm^{-1}) [37]. Upon undergoing the α → β phase transition, the XeF_2 molecules remain as bridging molecules (vide infra), but the oxygen atom interaction(s) with the XeF_2 molecules are considerably weaker, accounting for why ν(XeO) (920, 924 cm^{-1}) is very similar to the gas-phase value (928 cm^{-1}). The polarization of electron density towards oxygen would render the Xe(VI) atom more positive and the Xe(VI)–F bonds more covalent in the α-phase (575 cm^{-1}) relative to those of β-$XeOF_4 \cdot XeF_2$ (550, 554, 560, 564, cm^{-1}).

The observation of only one band at 503 cm^{-1} and assigned to XeF_2 in β-$XeOF_4 \cdot XeF_2$ reveals that the XeF_2 molecules are symmetrically (or near-symmetrically) bridging. The fact that it occurs at higher frequency than in α-$XeOF_4 \cdot XeF_2$ (494 cm^{-1}) is also in agreement with the aforementioned hypothesis. In the absence of a significant interaction between oxygen and the xenon atom of XeF_2, Xe(II) is more positively charged in β-$XeOF_4 \cdot XeF_2$ which is accompanied by increases in the covalency of the Xe(II)–F bonds and $\nu(Xe_2F_5) + \nu(Xe_2F_5')$.

2.5. Computational results

The energy-minimized geometries of $XeOF_4 \cdot 4XeF_2$ (C_4) (Fig. 5a) and $2XeOF_4 \cdot XeF_2$ (C_{2h}) (Fig. 5b) were obtained and resulted in stationary points with all frequencies real at the PBE1PBE level of theory, and two imaginary frequencies at the B3LYP level. The energy-minimized geometries and vibrational frequencies of $XeOF_4$ (C_{4v}), (Tables S1 and S6) and XeF_2 ($D_{\infty h}$) (Tables S2 and S7), were also obtained at the B3LYP and PBE1PBE levels of theory for use as benchmarks.

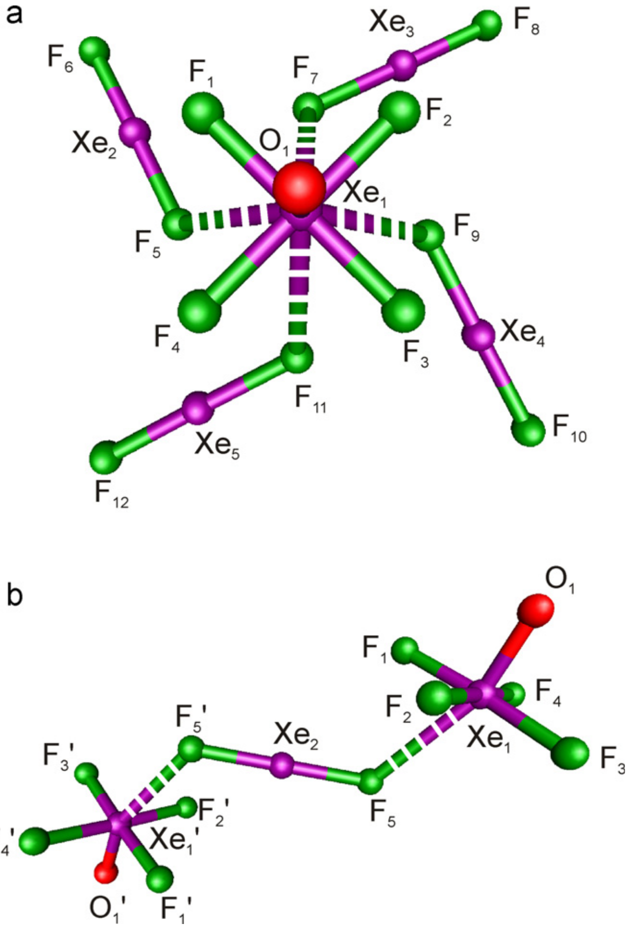

Fig. 5. Calculated PBE1PBE/aug-cc-pVTZ(-PP) gas-phase geometry for (a) $XeOF_4 \cdot 4XeF_2$ (C_4) and (b) $2XeOF_4 \cdot XeF_2$ (C_{2h}).

The structure of $XeOF_4 \cdot 2XeF_2$ was calculated to model the local XeF_2 environment in the crystal structure of α-$XeOF_4 \cdot XeF_2$. The XeF_2 molecule is symmetrically coordinated to two $XeOF_4$ molecules and the local symmetry of the XeF_2 molecule, including the Xe···F bridge interactions with $XeOF_4$, is C_s (see Section 2.3). The XeF_2 molecule is symmetrically coordinated to two $XeOF_4$ molecules, providing a local environment for the XeF_2 molecule that closely approximates the crystallographic structural unit.

The geometry of $XeOF_4 \cdot 4XeF_2$ (C_4 symmetry) was calculated to model the local environment of $XeOF_4$ in the crystal structure of α-$XeOF_4 \cdot XeF_2$. Each $XeOF_4$ molecule in α-$XeOF_4 \cdot XeF_2$ has four short contacts to fluorine atoms of an adjacent XeF_2 molecule (see Section 2.3). The calculated geometry of $XeOF_4 \cdot 4XeF_2$ consists of four XeF_2 molecules that are symmetrically coordinated to the $XeOF_4$ molecule from below the basal plane of its four fluorine ligands, providing a good approximation of the $XeOF_4$ environment in the crystal structure of α-$XeOF_4 \cdot XeF_2$.

2.5.1. Calculated geometries

The energy-minimized geometries of $2XeOF_4 \cdot XeF_2$ and $XeOF_4 \cdot 4XeF_2$ (Table 2) are similar at the PBE1PBE and B3LYP levels of theory. Although identical trends are expected at both levels, the values calculated at the PBE1PBE level provide better overall agreement with experiment and are explicitly referred to in the ensuing discussion.

2.5.1.1. $2XeOF_4{\cdot}XeF_2$. The calculated Xe_1–F_5 bond length (1.999 Å) is comparable to that of XeF_2 (2.014(5) Å) in α-$XeOF_4{\cdot}XeF_2$ and is slightly elongated when compared with that calculated for gas-phase XeF_2 (1.986 Å). The calculated $Xe{\cdots}F_5$ contact distance (2.890 Å) in $2XeOF_4{\cdot}XeF_2$ is significantly underestimated when compared with the experimental value (3.239(4) Å). The discrepancy may result from the simplified model which involves one $XeOF_4$ group coordinated to each fluorine ligand of XeF_2 instead of two $XeOF_4$ groups in the experimental structure, resulting in a shorter calculated $Xe_1{\cdots}F_5$ contact distance.

2.5.1.2. $XeOF_4{\cdot}4XeF_2$. The calculated Xe_1–O_1 and Xe_1–F_1 bond lengths of $XeOF_4{\cdot}4XeF_2$ (1.727 and 1.928 Å) are in good agreement with the experimental values for α-$XeOF_4{\cdot}XeF_2$ (1.729(7) and 1.900(3) Å) and the gas-phase microwave (1.70(5) and 1.95(5) Å) and electron diffraction (1.71(1) and 1.901(3) Å) structures of $XeOF_4$ as well as with the calculated gas-phase values for $XeOF_4$ (1.726 and 1.924 Å). The calculated O_1–Xe_1–F_1 bond angle of $XeOF_4{\cdot}4XeF_2$ (90.3°) is close to 90°, in agreement with the experimental O(1)–Xe(1)–F(1) bond angle of α-$XeOF_4{\cdot}XeF_2$ (89.2(1)°), but contrasts with the O–Xe–F bond angles calculated for $XeOF_4$ (92.0°). The slightly smaller O–Xe–F angle results from increased steric repulsion between the equatorial fluorine atoms of $XeOF_4$ and the fluorine atoms of the coordinated XeF_2 molecule. The $Xe_1{\cdots}F_5$ contacts of $XeOF_4{\cdot}4XeF_2$ (3.357 Å) are in good agreement with the experimental structure for α-$XeOF_4{\cdot}XeF_2$ (3.239(4) Å). The $Xe_1{\cdots}F_{5,7,9,11}$–$Xe_{2,3,4,5}$ angles of $XeOF_4{\cdot}4XeF_2$ (117.3°) are in very good agreement with the observed Xe(1)···F(5)–Xe(1) angle in $XeOF_4{\cdot}2XeF_2$ (116.8(1)°), again confirming that the model structure is reliable.

2.5.2. Charges, valencies, and bond orders

The Natural Bond Orbital (NBO) [43–46] analyses were carried out for the B3LYP- and PBE1PBE-optimized gas-phase geometries of $2XeOF_4{\cdot}XeF_2$ (Table S8), $XeOF_4{\cdot}4XeF_2$ (Table S9), $XeOF_4$ (Table S10), and XeF_2 (Table S11). Although all values are similar and because the PBE1PBE geometries better reproduce the experimental geometries (see Section 2.5.1), only the PBE1PBE values are discussed.

The natural population analyses (NPA) give positive charges of 3.17 and 3.18 for Xe(VI) of the $XeOF_4$ molecule in $2XeOF_4{\cdot}XeF_2$ and $XeOF_4{\cdot}4XeF_2$, respectively. The Xe(II) atom charges are 1.26 and 1.24, respectively. The charges on the F and O atoms bonded to Xe(VI) in $2XeOF_4{\cdot}XeF_2$ (F, −0.58, −0.59; O, −0.84) and $XeOF_4{\cdot}4XeF_2$ (F, −0.59; O, −0.85) and those of the F atoms bonded to Xe(II) (−0.62, −0.64, respectively) are also consistent with the polar covalent natures of the Xe–O and Xe–F bonds in the model structures.

The Xe–O (0.93) and Xe–F (0.39) bond orders in both model structures are essentially the same, indicating that the different coordination motifs of the $XeOF_4$ molecules have very little effect and are also very close to those obtained for $XeOF_4$ in the gas phase (0.94 and 0.40, respectively). The Xe–F bond order of the symmetrically coordinated XeF_2 (0.31) molecule of $2XeOF_4{\cdot}XeF_2$ is very similar to those of XeF_2 in the gas phase (0.29). The Xe–F bond orders in $XeOF_4{\cdot}4XeF_2$ are asymmetric (XeF_2, 0.28 and 0.31), where the smaller Xe–F bond order is associated with the fluorine bridge atom. The $Xe_1{\cdots}F$ bond orders in both structures are less than 0.04, and are again indicative of weak fluorine bridge interactions between $XeOF_4$ and XeF_2.

3. Conclusions

Although the ^{19}F and ^{129}Xe NMR spectra of XeF_2 dissolved in $XeOF_4$ do not provide any evidence for an associated complex in solution, two solid phases of the molecular addition compound, $XeOF_4{\cdot}XeF_2$, have been synthesized by the reaction of XeF_2 with $XeOF_4$. The X-ray crystal structure of the more stable α-phase shows that the XeF_2 molecules are symmetrically coordinated to four $XeOF_4$ molecules. The Xe(VI) atoms of the $XeOF_4$ molecules are, in turn, coordinated to four XeF_2 molecules resulting in a Xe(VI) coordination sphere that is based on a monocapped square antiprism. A high-temperature phase, β-$XeOF_4{\cdot}XeF_2$, has also been observed by low-temperature Raman spectroscopy in admixture with α-$XeOF_4{\cdot}XeF_2$; however, the instability of the β-phase has precluded its isolation and characterization by single-crystal X-ray diffraction. The Raman spectrum of β-$XeOF_4{\cdot}XeF_2$ indicates that $XeOF_4$ interacts less strongly with XeF_2 in the crystal lattice. The calculated structures of $2XeOF_4{\cdot}XeF_2$ and $XeOF_4{\cdot}4XeF_2$ have been used to provide close approximations of the local environments of the XeF_2 and $XeOF_4$ molecules in the experimental structures, allowing the vibrational modes of both molecular addition compounds to be described. The fluorine bridge interactions in α-$XeOF_4{\cdot}XeF_2$ are among the weakest known for compounds in which XeF_2 functions as a ligand, whereas such fluorine bridge interactions are considerably weaker in β-$XeOF_4{\cdot}XeF_2$.

4. Experimental

4.1. Apparatus and materials

Manipulations involving air-sensitive materials were carried out under anhydrous conditions as previously described [47]. All preparative work was carried out in 1/4-in. or 4-mm o.d. lengths of FEP tubing. The tubing was heat-sealed at one end and connected through 45° SAE flares to Kel-F valves. Reaction vessels were vacuum dried on a Pyrex vacuum line for 12 h and then transferred to a metal vacuum line where they were passivated with F_2 for 12 h, refilled with dry N_2, and placed in a drybox until used. All vacuum line connections were made by use of 1/4-in. Teflon Swagelok unions fitted with Teflon front and back ferrules. Xenon oxide tetrafluoride was synthesized by the hydrolysis of XeF_6 as previously described [48]. Xenon difluoride was synthesized by the reaction of Xe and F_2 gas as previously described [49].

4.2. Syntheses of α- and β-$XeOF_4{\cdot}XeF_2$

A fluorine-passivated 1/4-in. o.d. FEP reaction vessel was attached to a metal vacuum line and 0.1144 g (0.512 mmol) of $XeOF_4$ was condensed into the vessel. The reaction vessel was transferred to a nitrogen-filled drybox, cooled to −130 °C, and 0.0480 g (0.284 mmol) of XeF_2 was transferred into the reactor. The reactor and valve assembly were removed from the drybox and upon warming to 22 °C, a colorless solution resulted. The sample was quenched at −78 °C and a Raman spectrum was recorded, revealing a mixture of $XeOF_4$, α-$XeOF_4{\cdot}XeF_2$ (67%) and β-$XeOF_4{\cdot}XeF_2$ (33%). The sample was warmed to 22 °C, whereupon the majority of the mixture liquefied, leaving several crystallites suspended in the solution. The sample was rapidly quenched to −78 °C and a Raman spectrum was recorded revealing a mixture of predominantly α-$XeOF_4{\cdot}XeF_2$ (~95%) with some $XeOF_4$ and a small amount of β-$XeOF_4{\cdot}XeF_2$ (~5%). The sample was maintained at −78 °C for 20 h followed by recording its Raman spectrum which showed mainly α-$XeOF_4{\cdot}XeF_2$ with some $XeOF_4$. The reactor was transferred into a nitrogen-filled dry box and the reaction vessel was cooled to −130 °C and an additional 0.0400 g (0.236 mmol) of XeF_2 was added, giving a 1:1 stoichiometry. The reactor was removed from the drybox and upon warming to 50 °C formed a colorless solution. Regardless of whether or not the sample was gradually cooled or rapidly quenched, the only product observed by Raman spectroscopy was α-$XeOF_4{\cdot}XeF_2$ (26–28 °C). A third portion of XeF_2 (0.0867 g, 0.512 mmol) was added to the sample inside the drybox in a similar manner to give a 1:2 molar ratio of $XeOF_4$ to XeF_2. Warming of the sample to 50 °C with periodic vigorous mixing over 5 h resulted in only partial dissolution of XeF_2. A Raman spectrum of the product revealed a mixture of α-$XeOF_4{\cdot}XeF_2$ and XeF_2.

4.3. Raman spectroscopy

The low-temperature Raman spectra of α- and β-$XeOF_4{\cdot}XeF_2$ (−150 °C) were recorded on a Bruker RFS 100 FT Raman spectrometer using 1064-nm excitation and a resolution of 1 cm^{-1} as previously described [50]. The spectra were recorded using a laser power of 300 mW and a total of 300 or 1200 scans.

4.4. Nuclear magnetic resonance spectroscopy

4.4.1. NMR sample preparation

A solution of XeF_2 in $XeOF_4$ was prepared in a 4-mm o.d. FEP NMR tube fused to a 1/4-in. o.d. length of FEP tubing. Xenon difluoride (ca. 0.0203 g) was loaded into the sample tube inside a drybox and fitted with a Kel-F valve. The NMR tube was connected to a FEP vacuum submanifold that was, in turn, connected to a $XeOF_4$ storage vessel and ca. 0.5 mL of $XeOF_4$ was condensed onto XeF_2 at −196 °C. The NMR sample tube was then heat sealed under dynamic vacuum at −196 °C and stored at −196 °C until its ^{19}F and ^{129}Xe NMR spectra could be recorded. The sample was dissolved at room temperature just prior to data acquisition. For data acquisition, the 4-mm FEP sample tube was inserted into a 5-mm o.d. thin-wall precision glass NMR tube (Wilmad).

4.4.2. NMR instrumentation and spectral acquisitions

Fluorine-19 and ^{129}Xe NMR spectra were recorded unlocked (field drift <0.1 Hz h^{-1}) on a Bruker DRX-500 spectrometer equipped with an 11.744-T cryomagnet. The NMR probe was cooled using a nitrogen flow and variable-temperature controller (BVT 3000).

Fluorine-19 NMR spectra were acquired using a 5-mm combination $^{1}H/^{19}F$ probe operating at 470.592 MHz. The spectra were recorded in 64K memories with spectral width settings of 47 kHz and acquisition times of 0.65 s, and were zero-filled to 64K, yielding data point resolutions of 0.76 Hz/data point. Relaxation delays of 0.1 s were applied and 2700 transients were accumulated.

Xenon-129 NMR spectra were obtained using a 5-mm broadband inverse probe operating at 138.086 MHz. The spectra were recorded in 128K memories with spectral width settings of 1000 kHz and acquisition times of 0.65 s, and were zero-filled to 128K, yielding data point resolutions of 0.76 Hz/data point. Relaxation delays of 0.1 s were applied and 7000 transients were accumulated.

The pulse widths, corresponding to bulk magnetization tip angles of approximately 90°, were 8.5 (^{19}F) and 10.0 (^{129}Xe) μs. Line broadenings of 0.1 (^{19}F) and 2.0 (^{129}Xe) Hz were used in the exponential multiplications of the free induction decays prior to Fourier transformation.

The ^{19}F and ^{129}Xe spectra were referenced externally at 30 °C to samples of neat $CFCl_3$ and $XeOF_4$, respectively. The chemical shift convention used is that a positive (negative) sign indicates a chemical shift to high (low) frequency of the reference compound.

4.5. X-ray crystallography

4.5.1. Crystal growth

Crystals of α-$XeOF_4{\cdot}XeF_2$ were obtained from a sample comprised of 0.1358 g (0.802 mmol) of XeF_2 and 0.67 g (3.0 mmol) of $XeOF_4$ contained in a 1/4-in. o.d. FEP reactor equipped with a side arm and pressurized with one atmosphere of dry nitrogen. The reactor was warmed to 25 °C and a clear, colorless solution formed. Crystals were grown as previously described [2]. The reactor was placed in a horizontal position, distributing the liquid along the length of the reactor and was then cooled to −36 °C over a 1 h period, resulting in the growth of colorless plates over several hours. Crystals were isolated by decanting the solvent at −37 °C under dry nitrogen into the side arm of the FEP vessel, which was immersed in liquid nitrogen, followed by evacuation and vacuum drying of the crystalline product under dynamic vacuum at −40 °C. The side arm containing the supernatant was removed by heat sealing off this portion of the reaction vessel under dynamic vacuum at −196 °C. The crystalline sample was stored at −78 °C until a suitable crystal could be mounted on the diffractometer. A crystal of α-$XeOF_4{\cdot}XeF_2$ having the dimensions $0.04 \times 0.07 \times 0.13$ mm^3 was selected at -105 ± 3 °C and was mounted in a cold stream (−173 °C) on a goniometer head as previously described [50].

4.5.2. Collection and reduction of X-ray data

The crystal was centered on a Bruker Apex II diffractometer, equipped with a CCD area detector, controlled by the APEX II Graphical User Interface (GUI) [51], and a sealed tube source emitting Mo Kα radiation monochromated ($\lambda = 0.71073$ Å) by a graphite crystal was used. Diffraction data collection (−173 °C) consisted of a full ω rotation at $\chi = 0°$ (using 5×250) frames, followed by a ψ scans (1010) frames at various ψ and χ settings to fill the gaps. The crystal-to-detector distance was 4.882 cm, and the data collection was carried out in a 512×512 pixel mode using 2×2 pixel binning. Raw data was processed using APEX II v 2.1 [51], which applied Lorentz and polarization corrections to three-dimensionally integrated diffraction spots. The program, SADABS [52], was used for the scaling of diffraction data, the application of a decay correction, and an empirical absorption correction on the basis of the intensity ratios of redundant reflections.

4.5.3. Solution and refinement of the structure

The XPREP program [53] was used to confirm the unit cell dimensions and the crystal lattice. The solution was obtained by direct methods which located the positions of the atoms defining the α-$XeOF_4{\cdot}XeF_2$ complex. The final refinement was obtained by introducing anisotropic thermal parameters and the recommended weightings for all of the atoms. The maximum electron densities in the final difference Fourier map were located near the heavy atoms. All calculations were performed using the SHELXTL-plus package [53] for the structure determination and solution refinement and for the molecular graphics. The choice of space group was further confirmed using PLATON as implemented within the WinGX software package [54].

4.6. Computational methods

The optimized geometries, frequencies, and NBO valencies, bond orders, and NPA charges for XeF_2, $XeOF_4$, $2XeOF_4{\cdot}XeF_2$, and $XeOF_4{\cdot}4XeF_2$ were calculated using density functional theory (DFT) at the B3LYP and PBE1PBE levels using aug-cc-pVTZ basis sets [55]. Pseudo-potentials were used for xenon (aug-cc-pVTZ-PP). The combined use of aug-cc-pVTZ and aug-cc-pVTZ-PP basis sets is indicated as aug-cc-pVTZ(-PP). Quantum-chemical calculations were carried out using the Gaussian 03 [56] and Gaussian 09 [57] programs. The levels and basis sets were benchmarked by calculating the energy-minimized geometries and frequencies of XeF_2, (Table S7) and $XeOF_4$ (Table S6) and by comparison with the experimental values. The geometries were fully optimized starting from the crystallographic coordinates using analytical gradient methods. After optimization at one level of theory, the geometries were optimized at the other level of theory to ensure an equivalent energy-minimized geometry had been achieved. The vibrational frequencies were calculated at the B3LYP and PBE1PBE levels using the appropriate minimized structure, and the vibrational mode descriptions were assigned with the aid of Gaussview [58].

Acknowledgments

We thank the Natural Sciences and Engineering Research Council of Canada for the award of postgraduate scholarships (M.J.H.) and for support in the form of a Discovery Grant (G.J.S.), the Ontario Graduate Scholarship in Science and Technology and the McMaster Internal Prestige "Ontario Graduate Scholarships" Programs for support (D.S.B.), and SHARCNet (Shared Hierarchical Academic Research Computing Network; www.sharcnet.ca) for computational resources.

Appendix A. Supplementary data

Supplementary data associated with this article can be found, in the online version, at doi:10.1016/j.jfluchem.2011.05.010. The crystal structure of $XeF_2{\cdot}XeOF_4$ has been deposited with the FIZ Karlsruhe Inorganic Crystal Structure Database; number CSD-422962.

References

[1] A. Zalkin, D.L. Ward, R.N. Biagioni, D.H. Templeton, N. Bartlett, Inorg. Chem. 17 (1978) 1318–1322.
[2] J.F. Lehmann, D.A. Dixon, G.J. Schrobilgen, Inorg. Chem. 40 (2001) 3002–3017.
[3] J.F. Lehmann, G.J. Schrobilgen, J. Fluorine Chem. 119 (2003) 109–124.
[4] F.O. Sladky, P.A. Bulliner, N. Bartlett, J. Chem. Soc. A (1969) 2179–2188.
[5] R.J. Gillespie, B. Landa, Inorg. Chem. 12 (1973) 1383–1389.
[6] B. Frlec, J.H. Holloway, J. Chem. Soc., Dalton Trans. (1975) 535–540.
[7] R.J. Gillespie, D. Martin, G.J. Schrobilgen, J. Chem. Soc., Dalton Trans. (1980) 1898–1903.
[8] H. St, A. Elliott, J. Lehmann, H.P.A. Mercier, H.D. Jenkins, G.J. Schrobilgen, Inorg. Chem. 49 (2010) 8504–8523.
[9] G. Tavčar, M. Tramšek, T. Bunič, P. Benkič, B. Žemva, J. Fluorine Chem. 125 (2004) 1579–1584.
[10] M. Tramšek, B. Žemva, J. Fluorine Chem. 127 (2006) 1275–1284.
[11] T. Bunič, G. Tavčar, M. Tramšek, B. Žemva, Inorg. Chem. 45 (2006) 1038–1042.
[12] T. Bunič, M. Tramšek, E. Goreshnik, G. Tavčar, B. Žemva, Inorg. Chem. 46 (2007) 5276–5282.
[13] M. Gerken, P. Hazendonk, A. Iuga, J. Nieboer, M. Tramšek, E. Goreshnik, B. Žemva, S. Zheng, J. Autschbach, Inorg. Chem. 46 (2007) 6069–6077.
[14] T. Bunič, M. Tramšek, E. Goreshnik, B. Žemva, Solid State Sci. 10 (2008) 1511–1516.
[15] J.H. Holloway, G.J. Schrobilgen, Inorg. Chem. 19 (1980) 2632–2640.
[16] J.H. Holloway, G.J. Schrobilgen, P. Taylor, J. Chem. Soc., Chem. Commun. (1975) 40–41.
[17] J.H. Holloway, G.J. Schrobilgen, Inorg. Chem. 20 (1981) 3363–3368.
[18] P.A. Tucker, P.A. Taylor, J.H. Holloway, D.R. Russell, Acta Crystallogr., B 31 (1975) 906–908.
[19] B. Žemva, A. Jesih, D.H. Templeton, A. Zalkin, A.K. Cheetham, N. Bartlett, J. Am. Chem. Soc. 109 (1987) 7420–7427.
[20] D.S. Brock, J.J. Casalis de Pury, H.P.A. Mercier, G.J. Schrobilgen, B. Silvi, J. Am. Chem. Soc. 132 (2010) 3533–3542.
[21] D.S. Brock, J.J. Casalis de Pury, H.P.A. Mercier, G.J. Schrobilgen, B. Silvi, Inorg. Chem. 49 (2010) 6673–6689.
[22] N. Bartlett, M. Wechsberg, Z. Anorg, Allg. Chem. 385 (1971) 5–17.
[23] G.R. Jones, R.D. Burbank, N. Bartlett, Inorg. Chem. 9 (1970) 2264–2268.
[24] J.H. Burns, R.D. Ellison, H.A. Levy, Acta Crystallogr. 18 (1965) 11–16.
[25] R.J. Gillespie, G.J. Schrobilgen, Inorg. Chem. 15 (1976) 22–31.
[26] G.J. Schrobilgen, J.H. Holloway, P. Granger, C. Brevard, Inorg. Chem. 17 (1978) 980–987.
[27] T. Birchall, R.D. Myers, H. Waard, G.J. Schrobilgen, Inorg. Chem. 21 (1982) 1068–1073.
[28] A. Bondi, J. Phys. Chem. 68 (1964) 441–451.
[29] N. Bartlett, M. Gennis, D.D. Gibler, B.K. Morrell, A. Zalkin, Inorg. Chem. 12 (1973) 1717–1721.
[30] M.J. Hughes, H.P.A. Mercier, G.J. Schrobilgen, Inorg. Chem. 49 (2010) 3501–3515.
[31] B.E. Pointner, R.J. Suontamo, G.J. Schrobilgen, Inorg. Chem. 45 (2006) 1517–1534.
[32] M.J. Hughes, H.P.A. Mercier, G.J. Schrobilgen, Inorg. Chem. 48 (2009) 4478–4490.
[33] E.J. Jacob, H.B. Thompson, L.S. Bartell, J. Mol. Struct. 8 (1971) 383–394.
[34] N.J. Brassington, H.G.M. Edwards, D.A. Long, J. Chem. Soc., Faraday Trans. 2 (74) (1978) 1208–1213.
[35] H. Burger, R. Kuna, S. Ma, J. Breidung, W. Thiel, J. Chem. Phys. 101 (1994) 1–14.
[36] H.A. Levy, P.A. Agron, J. Am. Chem. Soc. 85 (1963) 241–242.
[37] P. Tsao, C.C. Cobb, H.H. Claassen, J. Chem. Phys. 54 (1971) 5247.
[38] P.A. Agron, G.M. Begun, H.A. Levy, A.A. Mason, C.G. Jones, D.F. Smith, Science 139 (1963) 842–844.
[39] F.O. Sladky, N. Bartlett, J. Chem. Soc. A (1969) 2188–2189.
[40] R. Hagiwara, F. Hollander, C. Maines, N. Bartlett, Eur. J. Solid State Inorg. Chem. 28 (1991) 855–866.
[41] A. Turičnik, P. Benkič, B. Žemva, Inorg. Chem. 41 (2002) 5521–5524.
[42] M. Tramšek, P. Benkič, B. Žemva, Solid State Sci. 4 (2002) 9–14.
[43] A.E. Reed, R.B. Weinstock, F. Weinhold, J. Chem. Phys. 83 (1985) 735–746.
[44] E.D. Glendening, A.E. Reed, J.E. Carpenter, F. Weinhold, In NBO Version 3.1, Gaussian Inc., Pittsburgh, PA, 1990.
[45] A.E. Reed, L.A. Curtiss, F. Weinhold, Chem. Rev. 88 (1998) 899–926.
[46] E.D. Glendening, J.K. Badenhoop, A.E. Reed, J.E. Carpenter, C.M. Bohmann, C.M. Morales, F. Weinhold, In NBO Version 5.0, Theoretical Chemical Institute, University of Wisconsin, Madison, WI, 2001.
[47] W.J. Casteel Jr., D.A. Dixon, H.P.A. Mercier, G.J. Schrobilgen, Inorg. Chem. 35 (1996) 4310–4322.
[48] G.A. Schumacher, G.J. Schrobilgen, Inorg. Chem. 23 (1984) 2923–2929.
[49] H.P.A. Mercier, J.C.P. Sanders, G.J. Schrobilgen, S.S. Tsai, Inorg. Chem. 32 (1993) 386–393.
[50] M. Gerken, D.A. Dixon, G.J. Schrobilgen, Inorg. Chem. 39 (2000) 4244–4255.
[51] *APEX2*, Release 2.0-2, Bruker AXS Inc., Madison, WI, 2005.
[52] G.M. Sheldrick, SADABS (Siemens Area Detector Absorption Corrections), version 2.10;, Siemens Analytical X-ray Instruments Inc., Madison, WI, 2004.
[53] G.M. Sheldrick, SHELXTL-Plus, Release 6.14, Siemens Analytical X-ray Instruments, Inc., Madison, WI, 2000–2003.
[54] L.J. Farrugia, J. Appl. Crystallogr. 32 (1999) 837–838.
[55] Basis sets were obtained from the Extensible Computational Chemistry Environment Basis Set Database, version 2/25/04, as developed and distributed by the Molecular Science Computing Facility, Environmental and Molecular Science Laboratory, which is part of the Pacific Northwest, Laboratory, P.O. Box 999, Richland, WA 99352.
[56] M.J. Frisch, et al., Gaussian 98, Revision A 11, Gaussian, Inc., Pittsburgh, PA, 2003.
[57] M.J. Frisch, et al., Gaussian 98, Revision A 11, Gaussian, Inc., Pittsburgh, PA, 2009.
[58] *GaussView*, release 3.0; Gaussian Inc., Pittsburgh, PA, 2003.